

Masters thesis

# **Investigation of Geiger cell prototypes for the SuperNEMO detector**

Thomas M. Conneely      Timothy D. Head

12th May 2008

School of Physics and Astronomy  
The University of Manchester

## **Abstract**

Drift cells in Geiger mode are used for three dimensional tracking of charged particles in large volumes. The performance of prototype drift chambers, for use as a tracking detector in the proposed SuperNEMO experiment, was investigated. Real-time data acquisition and analysis software was developed to assist in measurements. Ageing studies were performed to show that stable detector operation was possible with newly designed end-caps. During this investigation failure of the first 9-cell prototype resulted in the end-cap material being changed. The detector gas mixture was varied and the optimal quenching gas concentration of 2% or 3% was found. To determine the efficiency and effective width of a cell with diameter 44 mm data was taken and a simulation developed. The absolute efficiency of the cell is  $84 \pm 2\%$  and the best fit between data and simulation is obtained for an effective width of 5.27 cm.

# Contents

<b>1. Introduction</b>	<b>4</b>
1.1. Double beta decay . . . . .	5
1.2. The SuperNEMO experiment . . . . .	7
<b>2. Physics of drift cells in Geiger mode</b>	<b>9</b>
2.1. A basic drift cell . . . . .	10
2.2. Creation of the avalanche . . . . .	10
2.3. The propagating plasma . . . . .	11
2.4. The role of the quenching gas . . . . .	12
<b>3. Readout and signal analysis</b>	<b>13</b>
3.1. Readout . . . . .	13
3.2. Anode signal analysis . . . . .	15
3.3. Cathode signal analysis . . . . .	16
3.4. Readout circuitry . . . . .	17
3.5. Position measurement . . . . .	18
<b>4. Studies of a real wire chamber</b>	<b>20</b>
4.1. Validating the new software . . . . .	20
4.2. Failure of the 9-cell prototype . . . . .	20
4.3. Dependence of the plateau on ethanol concentration . . . . .	22
<b>5. Determining absolute efficiency</b>	<b>24</b>
5.1. Experimental setup . . . . .	24
5.2. Simulation . . . . .	25
5.3. Method and data . . . . .	27
5.4. Discussion . . . . .	28
<b>6. Conclusion</b>	<b>31</b>
<b>A. Analysis software screenshots</b>	<b>32</b>

# 1. Introduction

The proposed SuperNEMO experiment will search for neutrinoless double beta decay ( $0\nu\beta\beta$ ), a process forbidden in the Standard Model due to violation of lepton number. If  $0\nu\beta\beta$  were to be observed, this would provide evidence for physics beyond the Standard Model. Confirming theories in the fields of astrophysics, neutrino, particle and nuclear physics. The Standard Model does allow a similar process, double beta decay ( $2\nu\beta\beta$ ), a rare decay with a lifetime of the order  $10^{20}$  years.  $2\nu\beta\beta$  is the simultaneous beta decay of two neutrons within a nucleus, as described by

$$2n \rightarrow 2p + 2e^- + 2\bar{\nu}_e.$$

Neutrinoless double beta decay is a hypothetical process which is described by

$$2n \rightarrow 2p + 2e^-$$

which is possible if a Majorana type neutrino is exchanged during the decay process. This is discussed in more detail in Section 1.1.

SuperNEMO aims to build upon data gathered by NEMO 3 and similar experiments, which have yet to indisputably observe  $0\nu\beta\beta$ . This project's aims were to characterise prototype tracking chambers for the SuperNEMO experiment. The tracking chamber is to be a gas drift chamber, operated in Geiger mode. In Section 1.2 an outline of the SuperNEMO construction and objectives is given.

Drift chambers operated in Geiger mode allow reconstruction of all three coordinates of a crossing particle, compared to only two in proportional mode. Furthermore, Geiger drift chambers can be read out by simple circuitry which makes them cheaper. The physics of the Geiger mode is covered in Chapter 2.

We developed data acquisition and analysis software, this was then used to measure key parameters of the detectors' operation. This allowed characterisation of the detectors' performance, and was used to provide data for all subsequent investigations. In order to understand the effects of the read-out circuit on the signals we developed a model of the circuit. The read-out circuit model and analysis software is described in Chapter 3.

Furthermore, we studied the ageing effects of a newly constructed prototype, discussed in Chapter 4. We also investigated the dependence of the Geiger plateau the concentration of ethanol in the gas mixture. Chapter 5 discusses the measurement and simulation work done in order to determine the absolute efficiency and active volume of a 44 mm cell to be used in the first large scale prototype.

## 1.1. Double beta decay

Neutrino oscillation experiments like SNO and KamLAND [7] have established that the neutrino mass is non-zero, however many properties of neutrinos have yet to be determined. The study of neutrinoless double beta decay ( $0\nu\beta\beta$ ) can provide insights in the following areas:

- the type of neutrinos: Majorana or Dirac;
- absolute neutrino mass scale: by measurement or limit setting;
- the type of the neutrino mass hierarchy: normal, inverted or quasi-degenerate.

The Standard Model allows neutrinos to be either of Dirac or Majorana type. If they are Majorana particles then they must have mass and be their own anti-particle. In the case of Dirac type, the neutrino and the anti-neutrino are different particles.

The process  $0\nu\beta\beta$  studied by NEMO 3, violates conservation of lepton number, a strictly conserved quantity in the Standard Model. This could provide a possible mechanism for explaining the matter/anti-matter asymmetry observed in today's universe [17].

Double beta decay is the transition of a nucleus with atomic number  $A$  and charge  $Z$  to a nucleus with charge  $Z + 2$ ,

$$(A, Z) \rightarrow (A, Z + 2) + 2e^- + 2\bar{\nu}_e$$

emitting two anti-neutrinos and two electrons. It was proposed by Göpper-Mayer [9] in 1935 and was first observed in 1950 by Inghram and Reynolds [10]. A Feynman diagram of this process is shown in Figure 1.1(a).

In order for double beta decay to take place, single beta decay has to be highly suppressed energetically. For a nucleus with atomic number  $Z$  normal  $\beta$  decay is energetically forbidden, if the binding energy of the daughter nucleus (with atomic number  $Z + 1$  for  $\beta^-$  decay) is less than that of the parent. For double beta decay the daughter

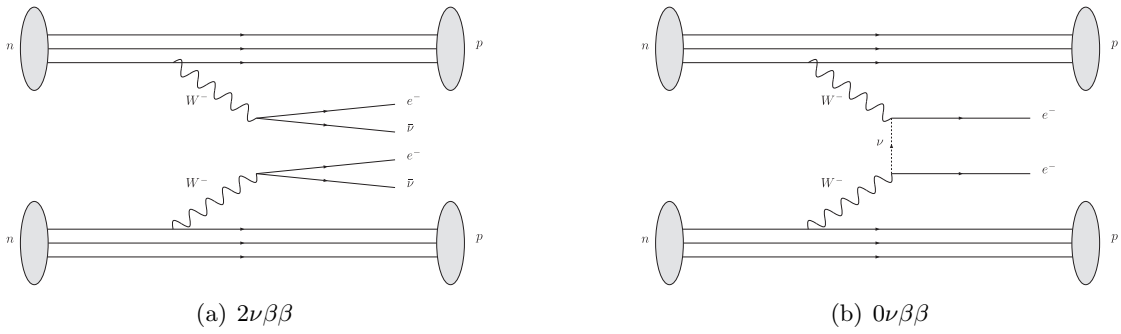


Figure 1.1.: The Feynman diagram on the left shows normal double beta decay and the one on the right neutrinoless double beta decay.

nucleus has atomic number  $Z + 2$ , hence for double beta to be allowed there must be a suitable nucleus with  $Z + 2$  and a lower binding energy. There are sixty nuclei that fit these criteria, but only ten have so far been observed to undergo double beta decay. These are  $^{48}\text{Ca}$ ,  $^{76}\text{Ge}$ ,  $^{82}\text{Se}$ ,  $^{96}\text{Zr}$ ,  $^{100}\text{Mo}$ ,  $^{116}\text{Cd}$ ,  $^{128}\text{Te}$ ,  $^{130}\text{Te}$ ,  $^{150}\text{Nd}$  and  $^{238}\text{U}$  [4].

As  $2\nu\beta\beta$  requires simultaneous decay of two nucleons, it is an extremely rare event, with lifetimes of the order of  $10^{20}$  years. The half-life can be calculated from

$$\left(T_{1/2}^{2\nu}\right)^{-1} = |M_{2\nu}|^2 \times G^{2\nu}(Z, Q)$$

where  $M_{2\nu}$  is the nuclear matrix element (NME) and  $G^{2\nu}$  is the phase space factor for the  $2\nu\beta\beta$  process which can be calculated exactly.

An alternative process, proposed by Furry in 1939 [8], is neutrinoless double beta decay ( $0\nu\beta\beta$ )

$$(A, Z) \rightarrow (A, Z) + 2e^-$$

in which no neutrinos are emitted. Although this process has so far not been observed, discovery claims have been made [12] but they remain disputed. A Feynman diagram of this process is shown in Figure 1.1(b).

The half-life of this process is given by

$$\left(T_{1/2}^{0\nu}\right)^{-1} = |M_{0\nu}|^2 \times G^{0\nu}(Z, Q) \times \langle m_{\beta\beta} \rangle^2$$

where  $M_{0\nu}$  is the relevant NME,  $G^{0\nu}$  is the phase space factor and  $\langle m_{\beta\beta} \rangle$  is commonly referred to as the “effective neutrino mass”, and is defined as

$$\langle m_{\beta\beta} \rangle = \sum_{i=1}^3 m_i U_{ei}^2$$

where  $m_i$  is the mass of neutrino type  $i$  and  $U_{ei}$  is the neutrino mixing matrix.  $0\nu\beta\beta$  is able to determine the type of neutrino mass hierarchy, as  $U_{ei}$  is sensitive to the relative masses of neutrinos [5].

The case in which the two lightest neutrinos have very similar masses and the third, heaviest, neutrino is well separated is referred to as “normal mass hierarchy”. An “inverted hierarchy” means that the lightest neutrino is clearly separated from the two other, heavier neutrinos. In this case the difference between the two heavy neutrino masses is small. In a “quasi-degenerate” mass hierarchy all neutrinos have roughly the same mass.

As neutrinos can not be detected directly one has to look at the energy spectrum of the emitted electrons to deduce properties of the neutrinos. In  $2\nu\beta\beta$  decay the available energy, i.e. the Q-value of the isotope, is shared between the electrons and neutrinos. As the neutrinos escape detection the sum of the energies of the electrons is a continuous distribution, as shown in Figure 1.2. In  $0\nu\beta\beta$  decay, however, only two electrons are emitted. Therefore, the sum of the electron energies equals the Q-value of the isotope giving a sharp peak, smeared out by the resolution of the detector. As  $2\nu\beta\beta$  decay is a background decay for the much rarer  $0\nu\beta\beta$  decay, an energy spectrum measured in a detector looks like that for  $2\nu\beta\beta$  with a slight excess of events close to the Q-value.

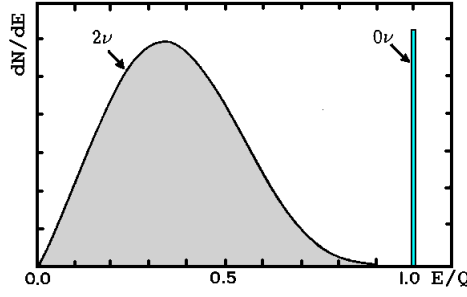


Figure 1.2.: The sum of the energies of double beta decay electrons emitted in  $2\nu\beta\beta$  and  $0\nu\beta\beta$  decay. The  $0\nu\beta\beta$  decay gives a peak at the end point (Q-values) energy of the continuous  $2\nu\beta\beta$  decay spectrum. The  $0\nu\beta\beta$  peak shown is exaggerated, a real signal would manifest itself as a slight modification to the tail of the distribution.

## 1.2. The SuperNEMO experiment

The SuperNEMO detector will be based on the technology of the Neutrino Ettore Majorana Observatory 3 (NEMO 3) experiment. The NEMO 3 experiment studies double beta decay and has been operating since February 2003 in the Fréjus Underground Laboratory in France. NEMO 3 aims were to directly detect the two electrons produced in double beta decay in order to observe or set a limit on  $T_{1/2}^{0\nu}$ .

SuperNEMO will continue to use the tracking and calorimetry approach of NEMO 3. There will be about 20 individual modules, shown in Figure 1.3, each containing about 5 kg of the isotope to be studied. The SuperNEMO detector will therefore contain around 100 kg of double beta decay isotopes, most likely  $^{82}\text{Se}$  or  $^{150}\text{Nd}$ . The tracking volume of each module will consist of over 2000 wire drift chambers and roughly 1000 scintillator blocks for the calorimeter. By capitalising on the modular design it is expected that the first modules will start taking data in 2010 and by 2015 SuperNEMO will operate with all twenty modules to reach a sensitivity of  $\langle m_{\beta\beta} \rangle < 50 - 90 \text{ meV}$ .

By using a tracker, calorimeter and magnetic field it is possible to reconstruct the trajectory of individual particles, find vertices, differentiate between positively and negatively charged particles, measure energies and the time of flight. This distinguishes NEMO 3 and SuperNEMO from experiments like Heidelberg-Moscow and Cuoricino [1] which are only able to measure the total energy deposited.

The tracking volumes surround the source foils, each one containing about 2000 drift cells operated in Geiger mode. The cells allow position reconstruction in all three dimensions, although a particle's energy cannot be measured.

The calorimeter is made up of large blocks of scintillator mounted on the side of the tracking volumes, with additional scintillators placed in the gaps between drift cells and on the top and bottom of each sector. The scintillators are read out by photomultiplier tubes with high radio purity. In addition to the energy, the scintillators measure the time of flight, crucial for reconstructing the radial position of a particle.

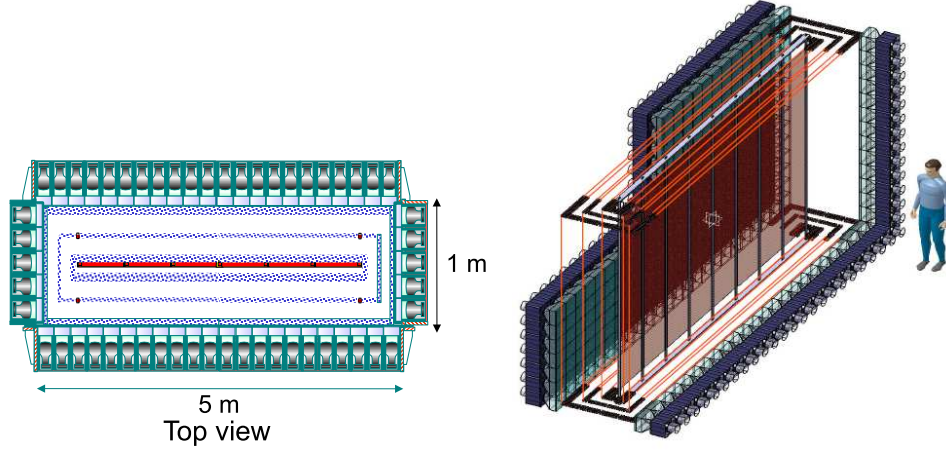


Figure 1.3.: A single SuperNEMO module. On the left picture the source foil is shown in red, in blue are the drift cells and in turquoise the calorimeter. The right picture shows a three-dimensional view of a module.

In order to distinguish  $e^+$  from  $e^-$  a magnetic field of 25 G parallel to the plane of the source foils is produced by a solenoid surrounding the detector. This also allows for efficient rejection of  $e^+e^-$  pair production. Crossing electrons are rejected using time-of-flight information from the scintillators. SuperNEMO will be placed underground, in a yet to be determined location, to reduce the background from cosmic rays. In addition, an iron shield reduces the number of  $\gamma$  rays entering the detector and a water shield captures fast and thermal neutrons.



## 2. Physics of drift cells in Geiger mode

This chapter discusses how drift cells operated in Geiger mode work. The beginning of the chapter gives an overview of the differences between the proportional mode and Geiger mode of operation. The basic layout of a cell is described in Section 2.1, followed by the mechanism of avalanche creation (Section 2.2) and a discussion of the propagation of the plasma along the anode wire (Section 2.3). The role and mechanism of the quenching gas is discussed in Section 2.4.

Both NEMO 3 and SuperNEMO use wire chambers operating in Geiger mode as the tracking detector. Wire chambers detect ionising particles, by collecting the trail of ions produced as the particle interacts with the detector gas. The more common mode of operation for a wire chamber is proportional mode. For proportional mode detectors the signal amplitude is dependent on a particles energy, and there is a very short dead time. This makes them attractive to experiments with a high rate of events, such as the LHC experiments. Proportional mode drift chambers require a sophisticated amplifier for reading out the signal due to its small amplitude, and a grid of wires for 3D reconstruction of particle positions.

When operating in Geiger mode a single ionisation event along the track of a crossing particle is enough to produce a signal which can be read out by a simple RC circuit. Typical signals are of the order of 100 mV and require no further amplification. A cell can be made of low radioactivity material and requires only little material in the tracking volume. The main advantage, however, is that a signal from a single wire is enough to reconstruct all three coordinates of a particles position. This is possible as the ionisation spreads along the wire and one can measure the time of arrival of the plasma at each end of the cell. Geiger drift chambers suffer from a long dead time ( $\sim 1$  ms), however, as the typical event rate in NEMO 3 and SuperNEMO is  $\sim 0.2$  Hz, this is not a problem.

The Geiger mode of operation occurs at high operating voltages, while at low voltages the cell is in proportional mode. The cell enters the Geiger plateau, in which the observed count rate is independent of the applied voltage. An example of count rate as a function of applied voltage is shown in Figure 2.1. The end of the plateau is characterised by the onset of self-triggering or continuous discharge/sparking which increases the rate dramatically.

Sufficiently below the starting voltage of the Geiger plateau the cell is in proportional mode, and the signals produced are too small to be detected, hence the count rate drops to zero. During the transition from proportional mode to Geiger mode, the start of the Geiger plateau, only a fraction of all events get detected due to incomplete propagation of the plasma along the anode wire.

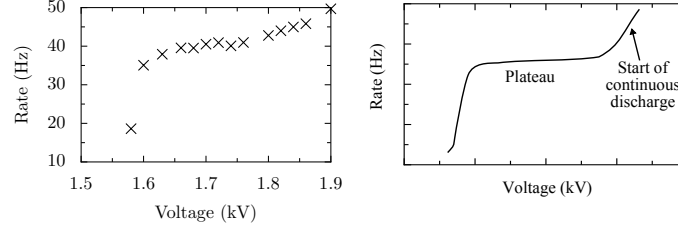


Figure 2.1.: Count rate as a function of applied anode voltage. On the left a typical plateau from a single cell prototype and on the right a theoretical plot.

## 2.1. A basic drift cell

An individual Geiger cell consists of a central anode wire surrounded by ground wires arranged in the shape of an octagon, as shown in Figure 2.2. Each cell in NEMO 3 is 2.7 m long and has a diameter of 3 cm. In order to detect the arrival of the plasma [2], cathode rings are mounted at each end of the cell. They are copper tubes of a diameter slightly less than that of the ground wires and are about 3 cm long. The rings are held at the same potential as the ground wires and once the plasma arrives inside the cathode ring it induces a signal in the shape of a sharp peak.

The gas mixture with which the prototype cells are filled is 95% helium, 4% ethanol and 1% argon. This is similar to the gas mixture used by NEMO 3. Helium is chosen as the main filling gas for its low  $Z$ -number, this reduces multiple scattering effects and energy loss of electrons as they traverse the Geiger cells. Ethanol is used as a quenching gas [2], which is discussed in Section 2.2.

An electric field is created by maintaining the anode wire at a high voltage ( $\approx 1600$  V) and the ground wires at ground level. Close to the anode the ionisation electrons gain sufficient energy between collisions in order to ionise or excite further gas molecules. This exponentially growing process creates an avalanche of electrons, which ultimately leads to an induced current in the anode wire. The creation of an avalanche is described in more detail in Section 2.2. The ions created in this avalanche drift slowly, compared to the electrons (typically  $0.1 \text{ cm } \mu\text{s}^{-1}$  compared to  $100 \text{ cm } \mu\text{s}^{-1}$  [19]), towards the cathode wire.

## 2.2. Creation of the avalanche

A particle crossing the active volume of a Geiger cell ionises a small number of the helium atoms. The free electrons produced drift towards the anode wire due to the potential maintained across the cell. The electric field in the Geiger cell accelerates the electrons so that they acquire enough momentum to ionise further gas molecules. This creates an avalanche of electrons, drifting towards the anode wire. Within the avalanche, on average one or more photons UV photons are emitted due to excited molecules returning to the ground state. These photons have a short range and enough energy to ionise further gas

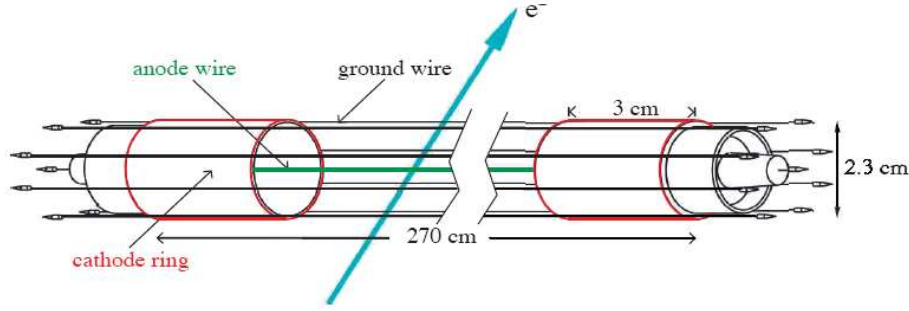


Figure 2.2.: A basic Geiger cell. The central wire is the anode, surrounded by eight ground wires. At the ends of the cell the two cathode rings are shown. [2]

molecules. As the avalanche progresses, an exponentially growing number of positive ions and electrons are produced close to the anode wire.

For the duration of the initial avalanche the ions can be considered stationary and the electrons are pinned to the anode wire. A typical avalanche takes of the order  $10^{-8}$  s in which the ions move  $\approx 10 \mu\text{m}$  [19], compared to a wire diameter of  $50 \mu\text{m}$ . As the ions accumulate around the anode they screen the field seen by other electrons close to the wire. However, far away from the anode the field remains the same as the positive charge of the ions cancels that of the electrons.

This reduction of the field has the effect of reducing the number of ion pairs created, as the electrons have less momentum. Consequently the average number of photons created in each avalanche falls to zero and no new avalanches are created. Wilkinson (1992) [20] contains a detailed discussion.

### 2.3. The propagating plasma

As mentioned previously, the positive ions can be considered to be stationary, this means that the electric field is reduced in a small area along the anode wire. Outside of this “burnt out” region there are no positive ions or electrons shielding the anode wire’s electric field.

Some of the photons created in the initial avalanches are emitted far enough along the wire to create electrons in the regions of high electric field on either side of the burnt out region, created by the initial avalanche. This causes the avalanche breeding process to move along the wire, away from “burnt out” regions, towards the ends of the wire chamber.

Even though the number of photons produced by each avalanche is subject to statistical fluctuations, the process of the avalanches spreading along the wire can be considered smooth and propagating at a constant velocity. This allows reconstruction of the position of the initial avalanche, from measuring the arrival times of the plasma at each end of the wire chamber.

## 2.4. The role of the quenching gas

When a helium ion reaches the cathode surface it is neutralised and left in an excited state. It then relaxes back to its ground state by emitting a photon. If the energy of the photon is greater than the workfunction<sup>1</sup> of the cathode material it is possible that a further electron is liberated from the cathode. This electron then seeds a new avalanche, which in turn produces further ions and the cell goes into continuous discharge mode. There are two possibilities to prevent this:

1. external quenching; or
2. internal/self quenching.

External quenching is achieved by reducing the high voltage applied to the anode after the beginning of the first avalanche and so reducing the electric field. However, this increases the dead time of the cell as all ions have to be neutralised before the high voltage can be increased again.

A self-quenching counter has a small amount of a polyatomic substance added to its gas, to absorb excess UV photons. Organic molecules are popular choices and ethanol is used both in NEMO 3 and our studies. The exact mechanism by which these polyatomic molecules suppress continuous discharge was not understood for a long time.

The two properties that make a good quenching gas are: photo-decomposition upon absorption of a UV photon and lower ionisation potential than helium, the fill gas [14].

Some of the UV photons created during avalanches are absorbed by the ethanol. This excites the ethanol molecule to a higher energy state, this state will then decay via photodissociation, where the molecule breaks apart. Ethanol is an effective quenching gas as it has many rotational and vibrational levels, leading to a wide and diffuse absorption spectrum in the UV range.

Also, as ethanol has a lower ionisation potential than helium, ionised helium atoms will interact via charge exchange with ethanol molecules. In the avalanche helium ions are produced which slowly drift towards the cathode, undergoing charge exchange with the ethanol molecules. Decreasing the number of helium ions and increasing the number of ethanol ions. By the time the ions reach the cathode nearly all of them are ethanol and all the helium ions have been neutralised. The ethanol molecules then decompose instead of emitting a photon when they neutralise close to the cathode [13].

An unfortunate side-effect of quenching gases is that the decomposition products can be deposited on the anode wire, where complex polymers will form in the high electric field. This ageing effect can reduce the detector's efficiency, and lead to failure of the detector due to plasma propagation being interrupted by polymer deposits [11].

---

<sup>1</sup>The emitted photon has an energy of 24.5 eV for helium, compared to a workfunction of 4.7 eV of pure copper.

### 3. Readout and signal analysis

As previously highlighted, the main advantage of operating in Geiger mode over proportional mode is that one can obtain the longitudinal and radial position of the crossing particle from just one cell. In NEMO 3 this is done by measuring the arrival times of the plasma at the ends of a cell, however, it is also possible to use only the anode signal and one cathode ring [15]. While measuring the position accurately is important for the final detector there are several other properties of a cell which can be deduced from the full signals, these are listed in Table 3.1.

Table 3.1.: A list of observables which give information about properties of the Geiger mode of operation.

<i>Observable</i>	<i>Provides information regarding</i>
Number of cathode pulses	Efficiency of plasma propagation
Amplitude of anode signal	Proportional to applied voltage, determined by properties of the readout network
Event rate	Beginning and end of the Geiger plateau
Propagation times	Determined by ethanol concentration and applied voltage
Rise time of anode signal	Charge exchange between ions, and their mobility in the gas

#### 3.1. Readout

The anode and two cathode signals are read out and digitised as three oscilloscope channels. A LabView program was developed to assist in full characterisation of the prototype detector.

The program analyses the raw signals, as represented in Figure 3.1, to measure the following times:

- $t_{a1}$  – start of a signal, which is the time the electrons ionised from the gas reach the anode wire
- $t_{a2}$  – beginning of the lowest part of the anode signal
- $t_{a3}$  – the time at which the plasma has arrived at one end of the cell
- $t_{a4}$  – the time at which the plasma has arrived at the other end of the cell
- $t_{c1}$  and  $t_{c2}$  – time at which the plasma arrives at cathode one and two

For the event depicted in Figure 3.1  $t_{a3} \approx t_{c1}$  and  $t_{a4} \approx t_{c2}$ , hence this event was closer to cathode one than cathode two; if the hit is closer to cathode two then  $t_{a3} \approx t_{c4}$  and  $t_{a4} \approx t_{c1}$ . As  $t_{a3}$  is the arrival time of the plasma at the end of the cell closest to the hit position at least one cathode signal is needed to resolve the resulting left-right ambiguity [15]. Figure 3.2 shows an oscilloscope trace of a real signal.

Using this timing information a number of parameters can be calculated that allow characterisation of the detector's performance in real time. These parameters are; longitudinal hit distribution, plasma propagation time and efficiency, anode signal amplitude

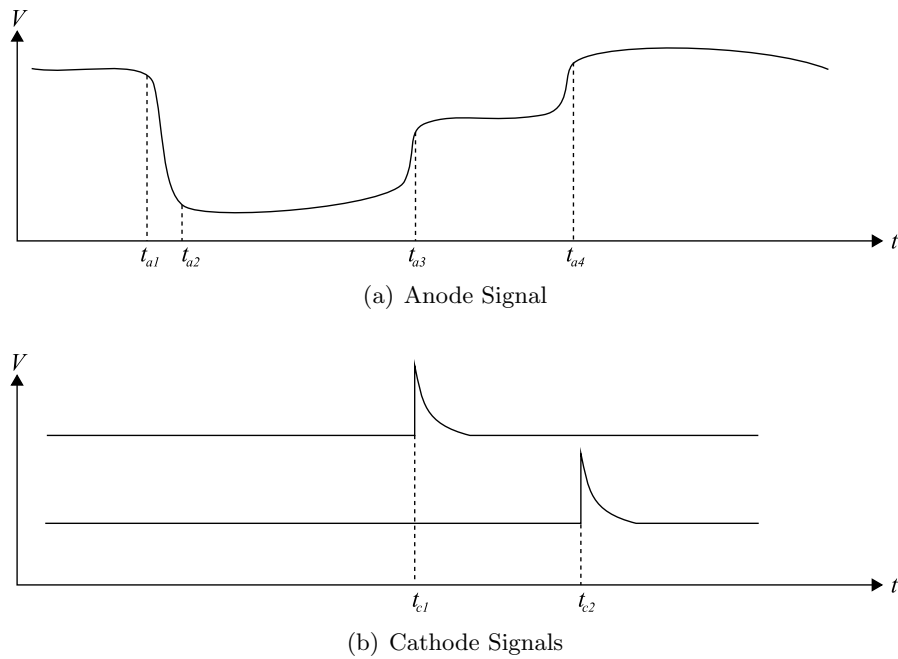


Figure 3.1.: A schematic event showing the signals recorded on the anode wire and the two cathode end rings.

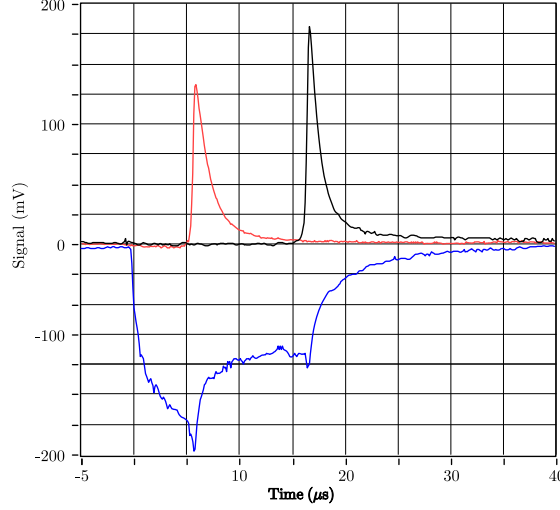


Figure 3.2.: An example of a real signal read out using the LabView acquisition software.

and drift time distribution. A screenshot of the acquisition software, showing histograms of these parameters is shown in Appendix A, Figure A.1. The software also allows individual events to be displayed for closer inspection and adjusting analysis thresholds, see Figure A.2.

### 3.2. Anode signal analysis

Initially a simple threshold technique was used to extract the four times from the anode signal. Two thresholds were defined, a high threshold  $l_1$  ( $\sim -10$  mV) and a low threshold  $l_2$  (the exact level is dependent upon the voltage supplied to the cell but is of the order  $-100$  mV). The first time  $t_{a1}$  is when the anode signal falls below  $l_1$  and  $t_{a2}$  is where  $l_2$  is crossed. Then  $t_{a3}$  is where the signal rises above  $l_2$  and  $t_{a4}$  is where  $l_1$  is exceeded. However, it proved difficult to set the thresholds appropriately to provide consistent results for different anode voltages.

The times to be measured using the anode signal correspond to large “steps” in the signal. The slope of the anode signal is small except for at these “steps”, by differentiating the signal the “steps” are turned into peaks, independent of the actual voltage level. Such a signal is much easier to consistently analyse with simple thresholds [15]. A “step” such as the one at  $t_{a3}$  will be a positive peak in the differential, whereas the step at  $t_{a1}$  will be a negative peak. In the case where more than two positive peaks were found the two closest to the cathode signals were selected.

For each event, the analysis software calculated the average anode amplitude  $V_{avg}$  (also known as the single plasma amplitude) using the relation

$$V_{avg} = \frac{1}{t_{prop}} \int_{t_{a1}}^{t_{a4}} V_a(t) dt$$

where  $V_a$  is the anode signal of the event and  $t_{prop} = t_{a3} + t_{a4} - 2t_{a1}$  is the total time for the plasma to propagate along the anode wire, and is equivalent to the total duration of the anode signal. Anode amplitude provides a measure of field stability, as fluctuations in field strength would produce variations of  $V_{avg}$ . For a given operating voltage the average voltage is a quantity which should not vary, hence a histogram of  $V_{avg}$  will show a sharp peak. This also allows one to determine how  $V_{avg}$  varies with operating voltage.

In practice  $t_{prop}$  was calculated from the cathode signals, using the relationship

$$t_{prop} = t_{c1} + t_{c2} - 2t_{a1}$$

as described in Section 3.3. This was necessary at low operating voltages due to the small anode signal amplitude, which made accurate analysis difficult. As the cathode signal amplitude does not vary greatly with cell voltage, accurate times could be measured, allowing correct calculation of  $V_{avg}$  for events at low operating voltages. Hence, a histogram showing  $t_{prop}$  for many events was also shown, with the mean and standard deviation of each experimental run being recorded for characterisation of the detector.

### 3.3. Cathode signal analysis

When the plasma reaches each end a large spike of charge is collected by the cathode rings, from positive ions from the plasma.

When the plasma reaches an end-cap, the positive ions are collected by the cathode ring, where they recombine with an electron. This creates a measurable spike of current when the plasma reaches the end-caps, the signal detected from the readout electronics is shown in Figure 3.1(b). Hence two times corresponding to the time of arrival at each end,  $t_{c1}$  and  $t_{c2}$ , can be measured. These times can then be extracted by applying a simple threshold crossing technique, as there is a large signal to noise ratio.

Crucially, these times can determine which end-cap was closest to a particle intersecting the cell; this cannot be determined using only the anode signal. Section 3.5 discusses how these two times can be used to measure the longitudinal position of an event.

An additional criterion was used to remove noise, which resulted in incorrect measurements. This was caused by the cathode signal crossing the threshold voltage multiple times. Hence, a minimum length for a cathode spike was set, this parameter could be adjusted for each experimental run, but a value of  $1\mu s$  was sufficient for most cases.

The cathode signal also provides a good trigger for counting events, due to its large amplitude and simple shape. As the LabView software is limited by the acquisition rate of the oscilloscopes, which is less than the rate of cosmic rays, it cannot calculate the event rate. However, the signal is big enough to be easily detected by a hardware discriminator and hence the rate can then be counted using a scaler.

By comparing the number of counts from each end it is possible to infer the stability of plasma propagation. Any interruption of the plasma as it travels along the anode wire would result in one cathode ring missing a spike. Hence, the software displays a histogram showing the number of events with two cathode spikes, one cathode spike and no cathode spikes for all acquired events.



### 3.4. Readout circuitry

As the signal generated in the drift cells depends strongly on the geometry, operating voltage and readout circuit used it is important to fully understand all factors contributing to the characteristics of the signal. A simulation of the signal generated by the cell with respect to geometry and operating voltage is under development by Steve Snow [18], however this simulation does not include the effects of the readout circuit.

The signals from current prototypes are read out by an oscilloscope connected to the cell via a readout circuit. The next prototype to be constructed will consist of 90 drift cells. Compared to previous single cell prototypes this one will have 180 channels that have to be read out and analysed in real time, consequently it is not possible to continue with the current setup of using oscilloscopes connected to a computer to read out and analyse the signals.

Instead each channel will be read out and digitised by an analogue to digital converter (ADC). In order to make efficient use of the ADCs precise knowledge of the amplitude and length of the anode and cathode signals is required.

The circuit was modelled using the SPICE simulation tool, a schematic of the full readout network is shown in Figure 3.3. A profile of the output voltage for the circuit was calculated by the simulation, from a current pulse generated using the previously mentioned signal generation simulation. Plots of the current pulse used as an input, simulated and real cathode signal are shown in Figure 3.4.

The delay introduced by the wire connecting the cell and readout box are unknown and hence were not included in the simulation. No significant change was observed when removing the delay in the wire connecting the readout box to the oscilloscope, so the effects are negligible. The ends of the drift cell are connected to the readout box by different lengths of cable with capacitances: 543 pF and 281 pF for the long and short wire respectively. Figure 3.4 shows the predicted signal for a cathode. Whilst the overall shape of the signal is easily reproduced by considering the components in the “readout box”, this grossly over estimates the amplitude of the signal. The effect of the capacitance introduced by the cables used to connect the cell to the “readout box”

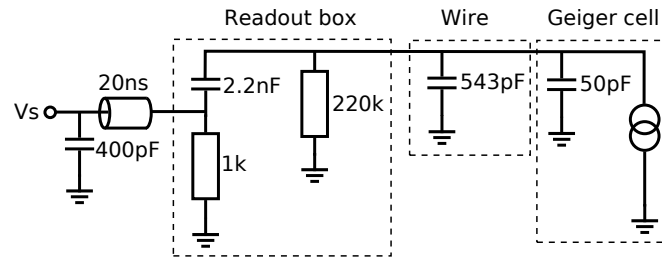


Figure 3.3.: Schematic of the full readout network. The Geiger cell is modelled as a current source. The wires connecting the readout circuit to the cell and to the oscilloscope are modelled as capacitors with capacitances as measured in the lab.

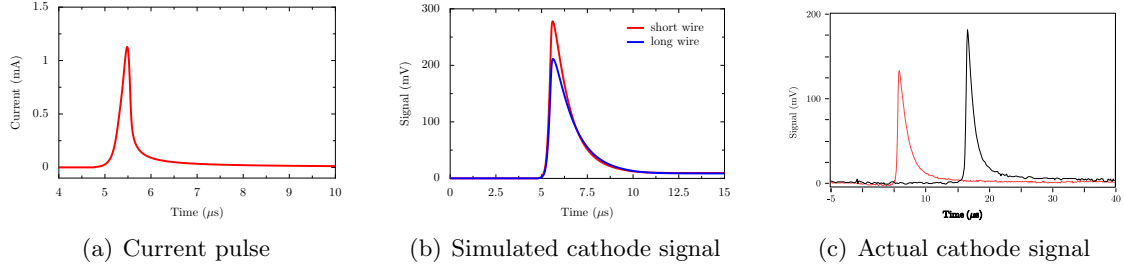


Figure 3.4.: (a) shows the current profile used as an input to the simulation, (b) predicted cathode signals for each end of a drift cell, (c) a signal measured for a typical event (the difference in amplitude is due to the different cable lengths used for both simulated and real data).

and to the oscilloscope is to reduce the amplitude significantly. After accounting for all electrical components the output of both simulations agrees to within a factor of two with signals observed in the laboratory. The discrepancy between the circuit simulation and an actual cathode signal is most likely due to the current profile used as an input, as the mechanism that produces the cathode signal is not fully understood.

### 3.5. Position measurement

The radial position can not be measured directly, instead the drift time is measured, which is given by

$$t_{drift} \equiv t_{a1} - t_0 = \int_0^{r_{hit}} \frac{dr}{v_{drift}(r)}$$

where  $r_{hit}$  is the distance from the point of ionisation to the anode wire, as illustrated in Figure 3.5(a). The start of the anode signal,  $t_{a1}$  and  $t_0$  is the time at which the particle enters the cell measured using scintillators, as indicated in Figure 3.1. The electric field is proportional to  $1/r$  close to the anode wire, hence  $v_{drift}$  is not a constant but depends on  $r$ .

The longitudinal position  $z$ , shown in Figure 3.5(b), can be found from the timing information contained in the anode signal. As discussed in Section 3.3, both the anode and cathode signals are needed to find the  $z$  position, as the closest end to an event cannot be determined otherwise. The program resolves the left-right ambiguity by calculating  $\Delta t_1 = |t_{c1} - t_{a3}|$  and  $\Delta t_2 = |t_{c1} - t_{a4}|$ . The longitudinal position, for the two cases  $\Delta t_1 < \Delta t_2$  and  $\Delta t_2 < \Delta t_1$ , is given by

$$z = L \left( \frac{t_{a3}}{t_{prop}} \right), \quad z = L \left( \frac{t_{a4}}{t_{prop}} \right)$$

respectively, where  $L$  is the total length of the cell and  $t_{prop}$ .

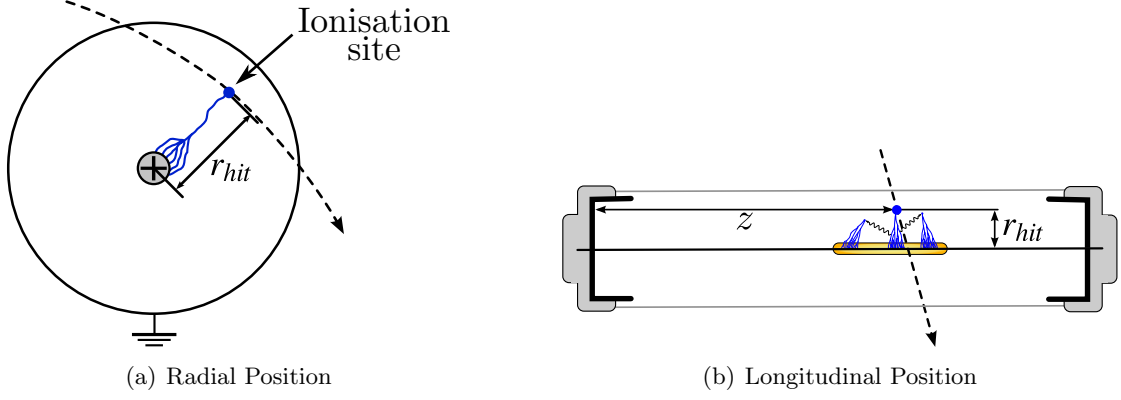


Figure 3.5.: For Geiger mode detectors, both longitudinal and radial position can be reconstructed

Therefore the position is calculated purely from times obtained from the anode signal. The position can also be found from the two cathodes only and is given by  $z = L(t_{c1}/t_{prop})$ . The resolution of the longitudinal position is given by

$$\sigma_z = \frac{L\sigma_t}{t_{prop}}$$

where  $\sigma_t$  is the standard deviation obtained from the distribution of total propagation times  $t_{prop}$ .

## 4. Studies of a real wire chamber

### 4.1. Validating the new software

In order to validate the data acquisition software and confirm previous research data was taken to study the propagation time and charge generated as a function of applied voltage. Figure 4.1 shows some examples of the collected data, taken on four different days.

The first set of data collected deviates slightly from the other results as the detector gas may not have had enough time to flush all contaminants (e.g. oxygen) from the chamber. All other sets of data agree closely with each other, with a region of stable operation in the range 1.55–1.65 kV.

The propagation time is inversely proportional to voltage in the region of the Geiger plateau. This would imply, as expected, that the propagation velocity is linear with respect to voltage. The anode signal amplitude plot also indicates a linear relationship, this is typical of all the prototypes tested using the analysis software.

### 4.2. Failure of the 9-cell prototype

Initially studies began using the three metre prototype detector which contained 9 individual Geiger cells. Each cell was constructed using a plastic end-cap to hold the anode wire and 10–12 ground wires in an octagonal arrangement, with the anode wire at the centre. The end-cap also provided electrical contacts for each cell's power supply and read-out electronics.

Initially the detector operated stably at voltages above 1.5 kV, with clear Geiger pulses on the anode wire and a spike on each cathode ring. At this stage the Geiger plateau was found by taking count rates from each cathode ring at various voltages. This indicated that the prototype was operating efficiently in the region of 1.5–1.7 kV.

However, after two weeks of the detector being supplied with gas and used for data taking<sup>1</sup> the detector performances rapidly deteriorated, eventually leading to complete failure. At previously stable voltages, no Geiger pulses could be detected and large discharges ( $\sim 1$  V in amplitude) were visible on the anodes and cathodes.

As every cell in the detector was affected, the failure could not be due to interruption of plasma propagation by contaminants being deposited on an anode wire. Three theories were therefore proposed; either there was an unidentified gas-borne contaminant that somehow depleted the quenching gas (or acted as a quenching gas itself), or the alcohol was forming a film on the plastic end-caps, adversely affecting their resistivity. A further

---

<sup>1</sup>No power was supplied to the detector when no data was being taken.

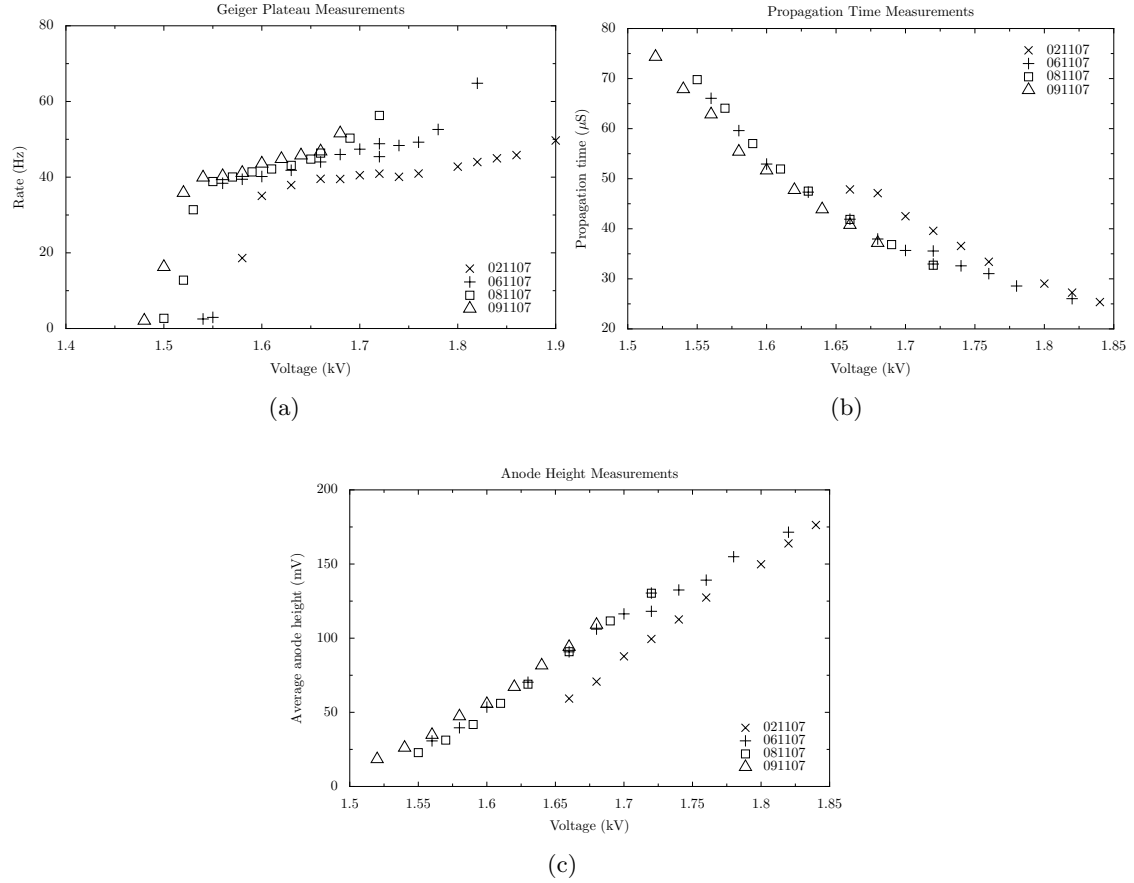


Figure 4.1.: Example plots showing results for count rate (a), propagation time (b) and anode signal amplitude (c). These results were collected using the analysis software to measure each data point, then plotted using another software package.

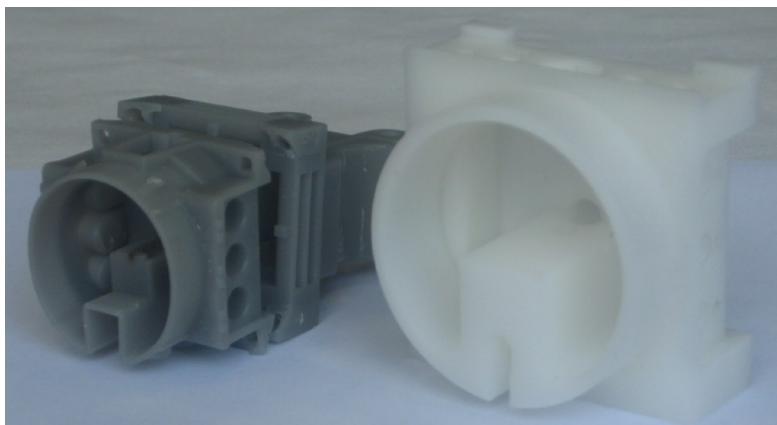


Figure 4.2.: On the left an end-cap as used in the 9-cell, which has cracked. On the right a new 44 mm end-cap, used in the new 9-cell and 44 mm single cell.

possibility would be an inherent flaw in the detector design, most likely due to the end-cap design creating regions of high field intensity, ultimately leading to the observed breakdown pulses.

The possible contaminant origins were unclear, but it was hypothesised that it was formed from a chemical reaction involving the breakdown products of alcohol in the high electric field, or a reaction involving the plastic end-caps which used a peculiar form of plastic due to the use of rapid prototyping in its construction.

To investigate the possibility of a gas borne contaminant, the gas output of the 9-cell detector was fed to an earlier single cell prototype. The 9-cell detector was then kept at a constant voltage, with the single cell operating in Geiger mode. The single cell performance was then monitored to check whether its performance would degrade due to the presence of a contaminant. As over a period of two weeks no deterioration was observed, it was concluded that a gas borne contaminant was not responsible for the 9-cell detector failure.

Upon disassembling the 9-cell detector it was found that the end-caps had become soft and cracks had developed, see Figure 4.2. This meant that the wires were no longer under tension. This resulted in a non uniform electric field along the cell which explains the deteriorating performance. New end-caps were machined from Delrin to replace the broken ones. A 9-cell detector with these end-caps has since operated well at voltages above 1.6 kV and after two months of operation shows no signs of ageing.

### 4.3. Dependence of the plateau on ethanol concentration

As the quenching gas is integral to efficient operation of the detector, it is important to fully understand how the detector behaves at various alcohol concentrations. This investigation was performed using the two wire cell. The quenching gas acts to remove UV photons from the detector, as discussed in Section 2.4. By increasing the concentration

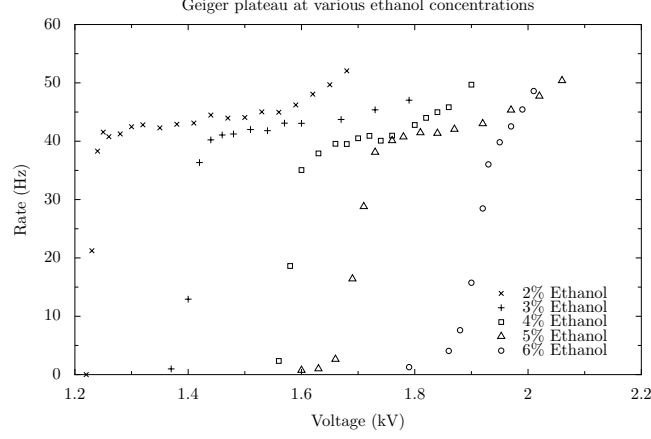


Figure 4.3.: The Geiger plateau at varying concentrations of ethanol

of ethanol more UV photons are removed. This reduces the likelihood of propagation, so the start of the Geiger plateau moves to a higher voltage. Conversely, by reducing the ethanol concentration less UV photons are removed, decreasing the plateau starting voltage and increasing the number of self-triggering events (i.e. a UV photon could travel a great enough distance from the original avalanche that it would trigger a secondary Geiger discharge, which could be mistaken for a second event).

The ethanol is dissolved in the gas by bubbling the helium and argon mixture through a container of ethanol. By controlling the temperature of the liquid ethanol, the gaseous concentration can be varied to the desired level. Hence, the temperature for a given concentration  $C_{eth}$  is given by

$$T = \frac{1554.3}{8.04494 - \log_{10}(760 C_{eth} P_{atm})} - 222.65$$

where  $P_{atm}$  is atmospheric pressure in mmHg and the constants are taken from Ref. [16]. It was possible to use five ethanol concentrations; 2%, 3%, 4%, 5% and 6% by volume.

Figure 4.3 shows the Geiger plateau for each of these concentrations. As expected for high concentrations, there is no longer an appreciable Geiger plateau at 6% ethanol. At low voltages UV photons are removed before they can initiate secondary avalanches and at high voltages the field around the anode wire is high enough to create self triggering events. At 2% and 3% ethanol the Geiger plateau covers a wider range of voltages than at 4% concentration. This would suggest the ideal concentration for the 2 wire cell would be 2% or 3%, as there is a larger region of stable operation. Whether this is true for the larger 9-cell prototype is unknown, hence it is proposed to further study the stability of the 9-cell at the concentrations 2%, 3% and 4% to find the optimal value.

## 5. Determining absolute efficiency

For SuperNEMO it has been decided to use drift cells of diameter 44 mm, as opposed to the smaller, 30 mm diameter cells used in NEMO 3. The cell diameter is a trade off between the total mass of material in the detector and position resolution. To test this new cell diameter a single cell prototype detector was constructed, using a scaled up end-cap design as used for the 9-cell Delrin prototype.

As only tens of gas molecules are ionised along the track of the crossing particle, it is important that ionisation electrons are not lost as they drift towards the anode. Gas impurities, such as Oxygen, may absorb the electrons, resulting in the particle not being detected. Hence, it is important to measure a cell's efficiency across its diameter.

### 5.1. Experimental setup

In order to determine when a muon had crossed the cell two scintillators were placed above and below the detector, as shown in Figure 5.1. If both scintillators register a signal in coincidence a particle has passed through the detector. For a 100% efficient drift cell each scintillator coincidence will produce a signal.

Each scintillator is 5 cm wide, 92 cm long and 3.6 cm high, two scintillators were combined to form one of length 184 cm. They are placed 56.5 cm vertically apart, centred on the drift cell. The drift cell is placed inside a cylindrical, stainless steel tank of outer diameter 21.6 cm, the thickness of the walls is approximately 5 mm. The drift cell was operated at 1.8 kV throughout the experiment. The Geiger plateau starts at 1.72 kV and at 1.8 kV the plasma propagates with near 100% efficiency along the anode wire.

To determine the background rate of scintillators hits due to noise, the random coincidence rate  $R_R$  was calculated. This is given by

$$R_r = 2R_1R_2\tau$$

where  $R_1$  and  $R_2$  are the rates of the top and bottom scintillators respectively and  $\tau$  is the length of the coincidence gate. The event rates measured in the top and bottom scintillator independently were  $R_1 = 2693.8$  Hz and  $R_2 = 201.5$  Hz respectively. While these rates are dominated by noise in the scintillators the rate of random coincidences is sufficiently low at 0.01 Hz, with  $\tau = 10$  ns [6].

By recording the rate of the Geiger cell at different offsets between the scintillators and drift cell's and by comparison with the simulation results, one can determine the effective width of the drift cell. Also the distribution of drift times (i.e. the time for the ionised electrons to reach the anode wire, given by  $t_{a1}$ ) was measured for each offset, and



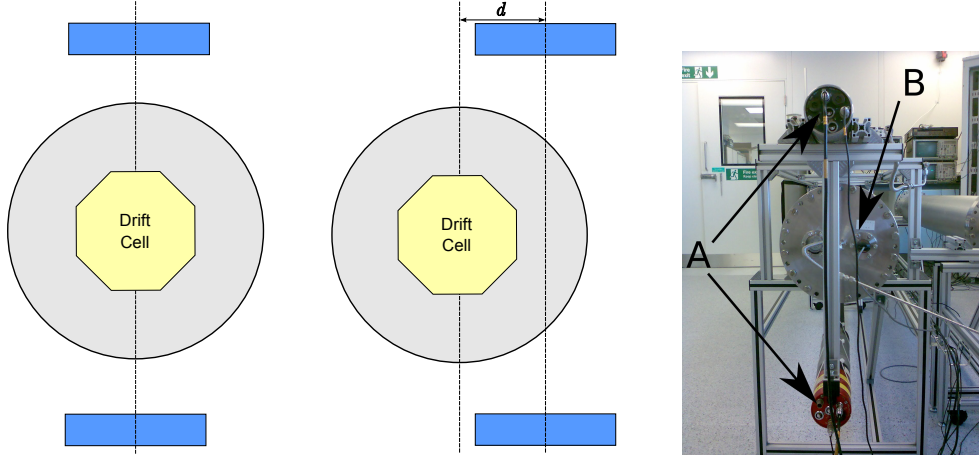


Figure 5.1.: A picture of the drift cell and scintillators in the lab. By increasing the offset  $d$  muons crossing certain parts of the drift cell can be selected. In the picture the two scintillators (A) and the steel tank (B) are shown.

calculated by the simulation. As the offset increases the number of events with small drift times should go to zero.

Muons are incident on the detector with an angular distribution which varies as  $\cos^7(\theta)$ , where  $\theta$  is the angle to the vertical [3]. This results in a triangular distribution of radial positions. To see this consider the geometry of the setup. The only muons able to create a hit at the edge of the cell are those which pass through the edge of the top and bottom scintillator, at right angle to the vertical. As we move towards the centre the angle of incidence which muons can make while still passing through both scintillators increases linearly, as show in Figure 5.2. The cosmic muon spectrum is assumed to be as given in [21, Ch. 24], with a mean muon momentum of  $4 \text{ GeV}/c^2$  and vertical flux of  $70 \text{ m}^{-2} \text{ s}^{-1} \text{ sr}^{-1}$ .

## 5.2. Simulation

The two main aims of developing the simulation were to predict the count rate and the drift time distribution for each scintillator offset. The count rate depends the width of the drift cell's active volume, i.e. the volume of the detector where ionisation events result in a measurable signal on the anode wire. This depends only on the geometry of the detector and cell. The drift time distribution depends on the electric field and drift velocities, however one can see exactly how far from the anode wire the events are. At big offsets a deficit of events with high drift times would indicate that the cell is less efficient further out.

The simulation generates particles, with uniformly distributed position above the the scintillators, and an angular distribution of  $\cos^7(\theta)$ , as given in [3]. For each event, if the particle intersected both scintillators and the closest approach to the anode wire

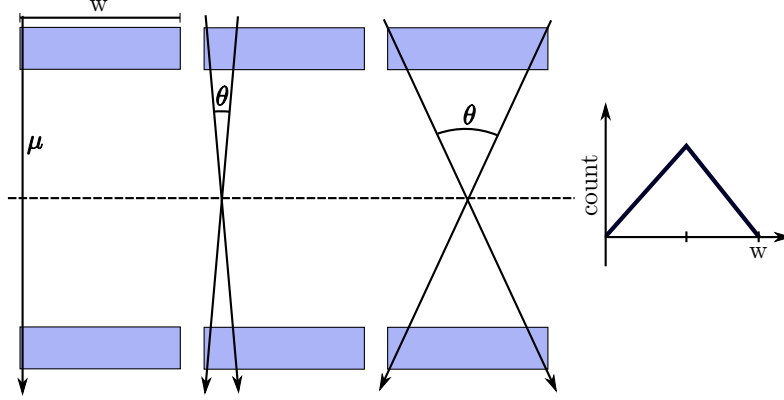


Figure 5.2.: Muons passing through both scintillators (blue) creating a hit at the edge, away from the edge and at the centre of the drift cell. Muons from a bigger range of incident angles contribute to hits at the centre then at the edge, resulting in a triangular hit distribution along the width of the cell.

was less than the assumed radius of the cell, the event was accepted and the radial position recorded. This means the cell assumes a uniform efficiency across its width. After an event had been accepted the value of the electric field at this location was looked up in a table provided by a FlexPDE model of the field. Using the field strength the corresponding drift velocity of electrons was found. The electron was then “drifted” towards the anode by multiplying the velocity by a small time step  $dt$ . At the new location the field strength was again looked up, the corresponding drift velocity found and these steps were repeated until the electron reached the anode wire. The total number of time steps  $dt$  taken gives the total drift time. The electric field data used and corresponding drift times are shown in Figure 5.3.

The simulation has two input parameters: the width of the drift cell and the coincidence rate of the scintillators  $R_s$ . The latter is used to convert the number of hits into a rate. If  $n$  scintillator hits were simulated, then the length of the run is  $t = \frac{n}{R_s}$  and all subsequent rates are calculated using this time.

A charged particle passing through steel undergoes many small angle scatters due to Coulomb scattering off the atomic nuclei. For small deflection angles Coulomb scattering is described by a Gaussian distribution. For heavy charged particles such as the muon, the width of the distribution is given by

$$\theta_0 = \frac{13.6 \text{ MeV}}{\beta c p} \sqrt{\frac{x}{X_0}} \left[ 1 + 0.038 \ln \frac{x}{X_0} \right]$$

where  $p$  and  $\beta$  are the particles momentum and speed,  $X_0$  and  $x$  are the radiation length and thickness of the material. For further details and Monte Carlo simulation techniques see Yao (2006) [21, Ch. 27]. To evaluate  $\theta_0$  the mean muon momentum in the laboratory was assumed to be  $> 1 \text{ GeV}$ ,  $\beta = 1$  and  $\frac{x}{X_0} = 0.284$ . This gives  $\theta_0 = 0.008$ , corresponding to a deflection of approximately 1.6 mm over the length of the diameter of the tank.

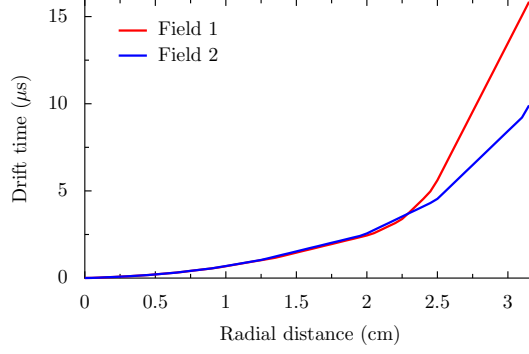


Figure 5.3.: Drift time as a function of radial distance for two different electric field data. The differences only become important for big radial distances, outside the nominal size of the cell of 2.2 cm.

### 5.3. Method and data

The event rate of the drift cell is measured by counting the number of cathode signals occurring within  $30 \mu\text{s}$  of a scintillator coincidence. At an operating voltage of 1.8 kV the propagation time along the anode wire is  $24 \mu\text{s}$ . This allows for a maximum drift time of  $6 \mu\text{s}$ , corresponding to a radial distance of 2.6 cm.

Measurements of the event rate in the drift cell were made for offsets in the range of  $-13 \text{ cm}$  to  $+8 \text{ cm}$ . This range was chosen as it covers the whole width of the steel tank and positions outside of the detector volume. The event rate therefore depends on the area of overlap between the scintillators and drift cell.

Data was taken without using the scintillators as a trigger and the drift cell detected muons at a rate of 80 Hz. The dead time of the 44 mm cell was measured to be  $800 \mu\text{s}$ . The measured coincidence rate of the scintillators is 0.53 Hz. The maximum event rate in the drift cell is approximately 0.3 Hz, as indicated in Figure 5.4.

For each offset the distribution of drift times was recorded, a selection of which is shown in Figure 5.5. For small offsets the data agrees very well with theoretical expectations, however, for large offsets there is an excess of events with low drift times.

In order to estimate the number of muons not detected due to the scintillators being longer than the drift cell only one pair of scintillators was used. They were placed so that they completely overlapped the drift cell. In this configuration 296 scintillator coincidences and 238 cathode signals were counted in 1200 s. This corresponds to a detection efficiency of 80%, compared to 60% for the full length scintillator setup. From this we estimate that  $1/4$  of all muons detected by the scintillators do not hit the drift cell. Due to the nonlinear efficiency of the scintillators along their length it is difficult to account more precisely for this effect.

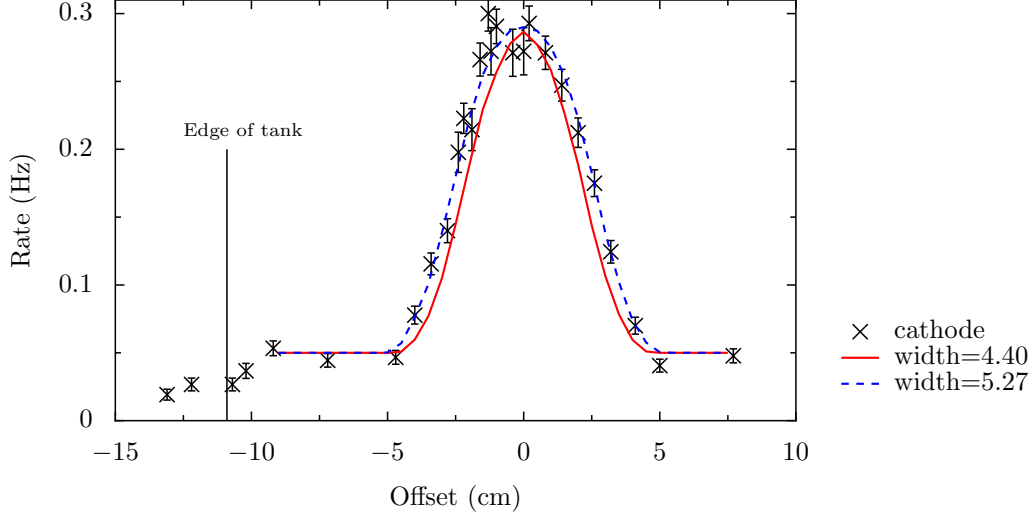


Figure 5.4.: Drift cell event rate as a function of scintillator offset. The lines show best fits for models with two different widths. The edge of the tank is marked and coincides with a drop in event rate. A further data point at an offset of  $-30$  cm confirms the low event rate outside the tank.

## 5.4. Discussion

The maximum event rate in the drift cell is 0.3 Hz, only about 60% of the coincidence rate of the scintillators. From previous experience with drift cells it seems unlikely that the cell has such a small efficiency. In this section several points, unrelated to the efficiency of the cell, which have an impact on the event rate of the drift cell and the observed drift times will be discussed.

The excess events with small drift times observed for large offsets (see Figure 5.5) can be reproduced in the simulation by assuming there is uniformly distributed background of 0.05 Hz across the detector. This is well supported by the 0.05 Hz signal that is seen up to the edge of the detector tank in Figure 5.4. Beyond this point the scintillators no longer overlap with the tank, and hence no events should be recorded in coincidence with the scintillators other than the 0.01 Hz expected due to random coincidences. The rate measured at an offset of  $-30$  cm agrees with measurements just outside of the tank.

The exact origins of this background signal remains unclear, the possibilities include radioactive decays in the detector or muons seeding showers due to interactions with the building structure and/or the detector tank.

Drift cells operated in Geiger mode have a dead time of about 1 ms. Muons passing through the detector when the read out is not triggered by a scintillator coincidence still result in a dead time. The total dead time due to  $n$  counts is  $nt_d$ , where  $t_d$  is the dead time of the cell. The number of events missed when triggering at a rate  $R$  is  $\Delta n = nt_d R$ . This means an event rate lower by the amount  $\Delta R = t_d R R_m$ , where  $R_m$  is the rate at which muons pass through the drift cell, will be measured. Using the muon flux, dead

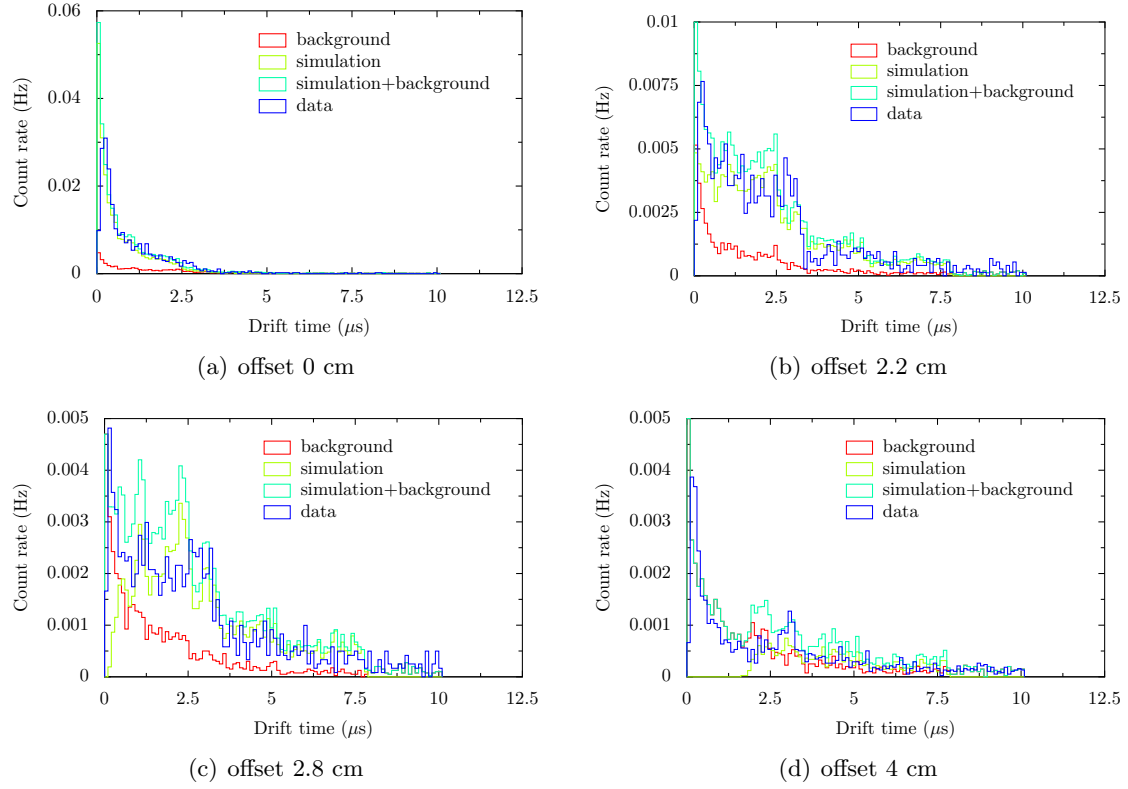


Figure 5.5.: Radial drift time distributions for offset: 0 cm, 2.2 cm, 2.8 cm and 4 cm. At small offsets the simulation agrees well with the data, however, at large offsets there is a excess of events with low drift times. By including a uniform background of rate 0.05 Hz the simulation can reproduce this excess of events.

Table 5.1.: The best fit for coincidence rate for different effective cell widths. An effective cell width of 5.27 cm gives the smallest  $\chi^2/\text{d.o.f.}$ , independent of the coincidence rate used.

width (cm)	coincidence rate (Hz)	$\chi^2/\text{d.o.f.}$
4.4	0.268	101.82/23
5.1	0.245	34.12/23
5.27	0.24	30.59/23
5.5	0.234	35.68/23

time and scintillator coincidence as given in the previous section  $\Delta R = 0.0367$  Hz.

Measuring the effective width of the drift cell involves two steps. First, a least-squares fit of the coincidence rate for each width was made. Second, the  $\chi^2$  of the best fit for each width were compared. The values are tabulated in Table 5.1, a width of 5.27 cm gives the overall best fit. In Figure 5.4 the rate distributions for the best fit for a cell of width of 4.4 cm and 5.27 cm are shown.

The absolute efficiency of the drift cell is then given by:

$$\epsilon = \frac{(4/3 R_a + \Delta R)}{R_s - R_r}$$

where  $R_a$  is the measured anode rate,  $R_s$  is the scintillator coincidence rate,  $\Delta R$  is the number of muons not detected due to dead time and  $R_r$  is the random coincidence rate. The measured anode rate is scaled by  $4/3$  to account for the number of events lost due to the scintillators being longer than the drift cell. For the 44 mm prototype the absolute efficiency is  $84 \pm 2\%$ .

## 6. Conclusion

The aim of this project was to characterise prototype tracking chambers for the SuperNEMO experiment. To achieve this we developed data acquisition software which we used to investigate:

- ageing effects
- dependence of the Geiger plateau on quenching gas concentration; and
- absolute efficiency and effective cell width of a new end-cap design.

For this we used three different prototypes, a two wire cell, a 9-cell and a single cell of width 44 mm. Signals from all prototypes were digitised by oscilloscopes and recorded to hard disk by a purpose built LabView program. The LabView software also analysed the raw oscilloscope data to extract information in real-time.

In addition to the raw timing information obtained from analysis of the signal, a number of performance parameters were calculated. This allowed the performance profile of a prototype to be quickly determined, and compared to previous data sets.

After failure of the first 9-cell prototype, investigations eliminated the possibility of a gas borne contaminant. This was explained when the 9-cell prototype was disassembled. As the end-caps, constructed using a rapid prototyping plastic, had reacted with the ethanol quenching gas and had cracked and turned soft. This resulted in new end-caps being made from Delrin, a durable, chemically inert and highly resistive plastic. Using the new end-caps we constructed a 9-cell prototype which continues to function reliably.

Results from varying the concentration of ethanol in the two wire cell show that the Geiger plateau position and width vary as expected; a lower concentration leads to an earlier starting voltage for the Geiger plateau. The results suggest that alcohol concentrations of 2% or 3% give a wider range of operating voltages than the 4% concentration used for the NEMO 3 detector however, the difference in operating stability is negligible.

The absolute efficiency of a 44 mm diameter prototype was measured using scintillators to trigger the readout when a particle crosses the detector. For the next SuperNEMO prototype the decision was made to use these bigger cells to reduce cost and material. We developed a Monte Carlo simulation of the detector, for comparison with data. This allowed us to perform a fit between data and simulation for different cell widths. A best fit between data and simulation was found for an effective width of 5.27 cm and we measure the absolute efficiency to be  $84 \pm 2\%$ . Furthermore there is no evidence for the cell being less efficient at large radii, meaning that 44 mm is a good choice for the next prototype.

# A. Analysis software screenshots

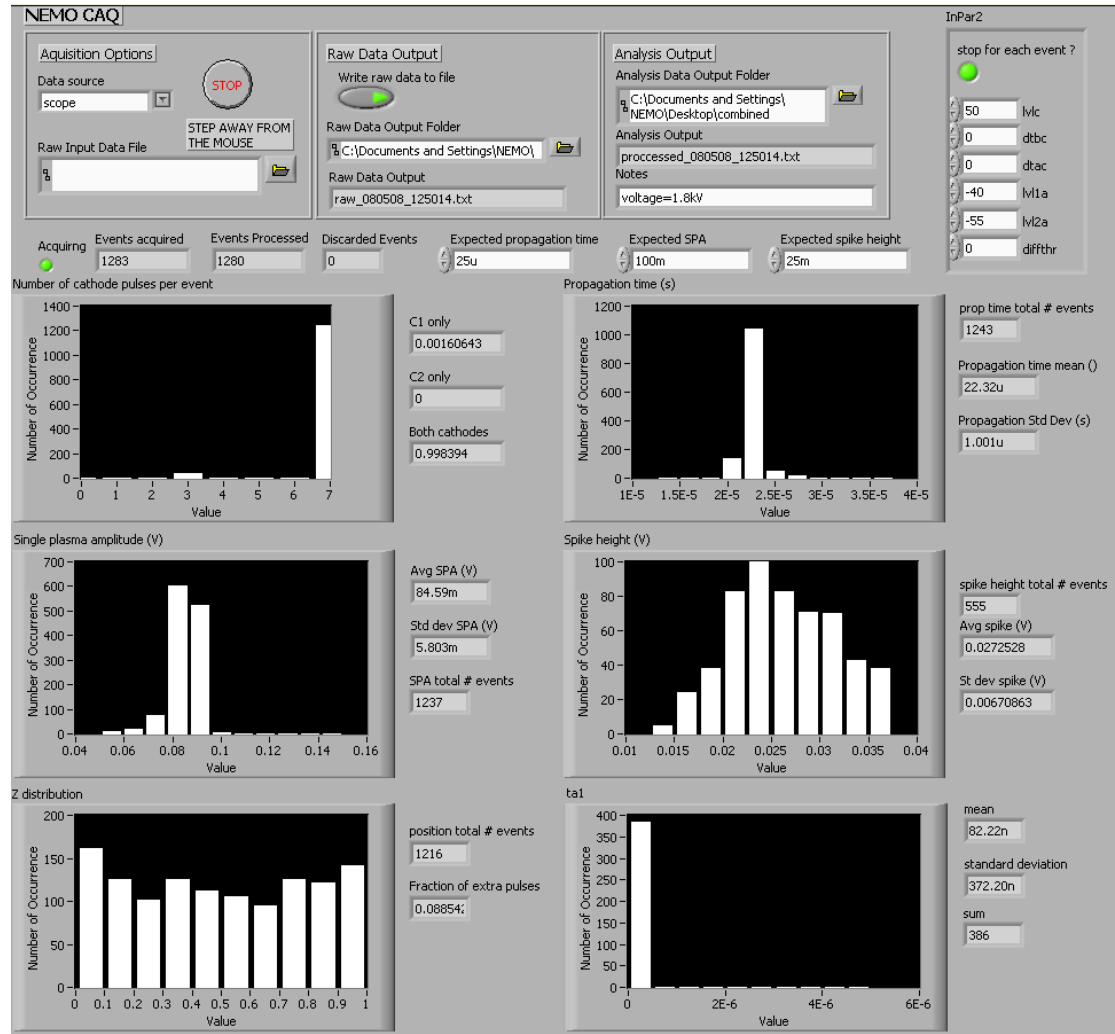


Figure A.1.: Main screen of the signal analysis software. Histograms shown (clockwise from top left): cathode efficiency, propagation time, spike height, drift time, hit position and anode amplitude.



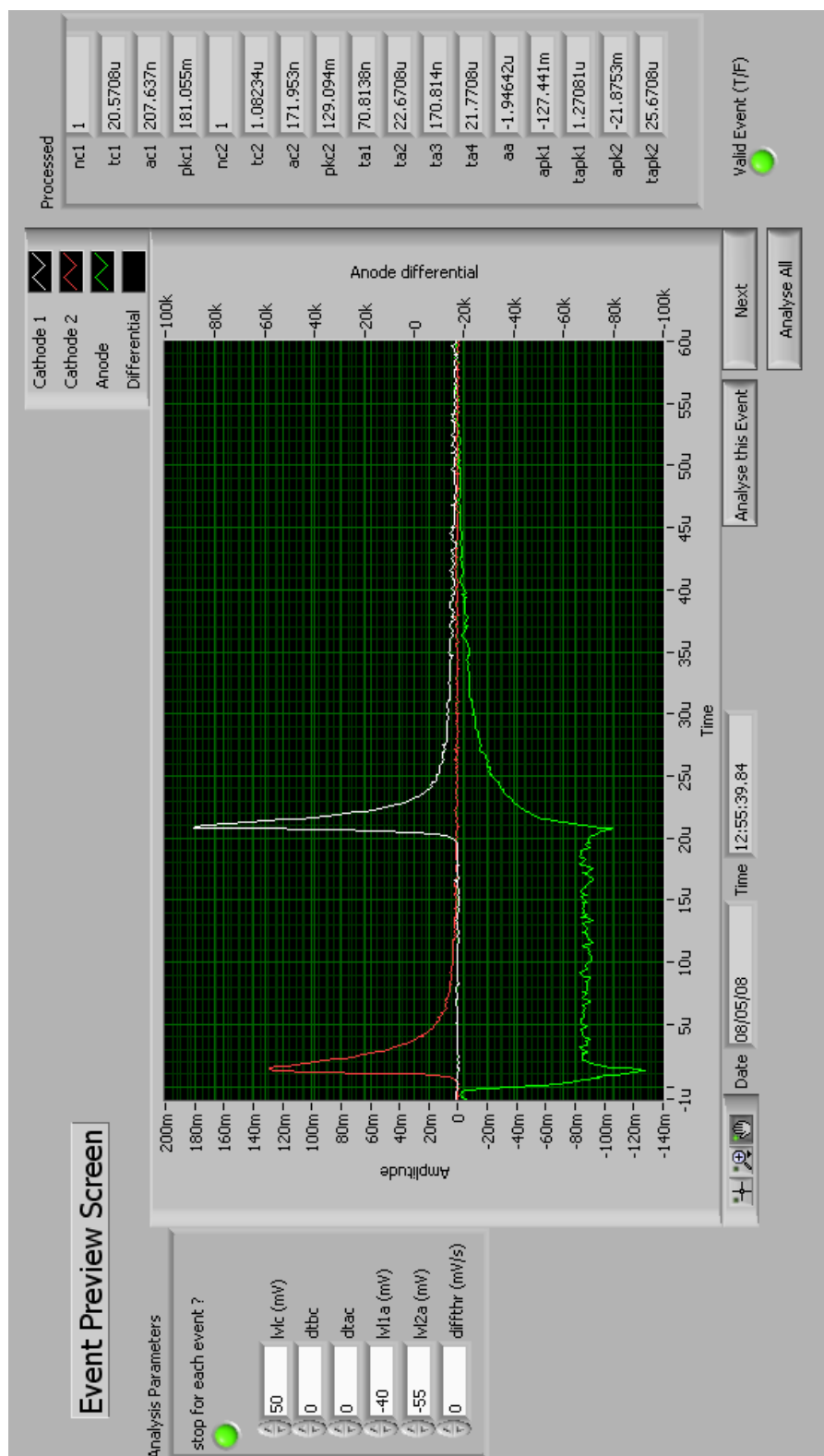


Figure A.2.: Event display of the analysis software. The cathode signals are shown in red and white, the anode signal in green.

# Bibliography

- [1] R. Ardito et al. CUORE: A cryogenic underground observatory for rare events. 2005, [hep-ex/0501010](#).
- [2] R. Arnold et al. Technical design and performance of the NEMO 3 detector. *Nucl. Instrum. Meth.*, A536:79–122, 2005, [physics/0402115](#).
- [3] M. Bahmanabadi, A. Anvari, Khakian, D. Purmohammad, J. Samimi, and Lamehi. A study of the effect of geomagnetic field on extensive air showers with small arrays. *Experimental Astronomy*, 13(1):39–57, February 2002, [doi:10.1023/A:1022038816555](#).
- [4] A. S. Barabash. Average (recommended) half-life values for two-neutrino double-beta decay. *Czech. J. Phys.*, 52(4):567–573, 2002, [doi:10.1023/A:1015369612904](#).
- [5] S. M. Bilenky, S. Pascoli, and S. T. Petcov. Majorana neutrinos, neutrino mass spectrum, *cp* violation, and neutrinoless double  $\beta$  decay: The three-neutrino mixing case. *Phys. Rev. D*, 64(5):053010, Aug 2001, [doi:10.1103/PhysRevD.64.053010](#).
- [6] C. Eckart and F. R. Shonka. Accidental coincidences in counter circuits. *Phys. Rev.*, 53(9):752–756, 1938, [doi:10.1103/PhysRev.53.752](#).
- [7] K. Eguchi et al. First results from KamLAND: Evidence for reactor anti-neutrino disappearance. *Phys. Rev. Lett.*, 90:021802, 2003, [hep-ex/0212021](#).
- [8] W. H. Furry. On transition probabilities in double beta-disintegration. *Phys. Rev.*, 56:1184–1193, 1939, [doi:10.1103/PhysRev.56.1184](#).
- [9] M. Goeppert-Mayer. Double beta-disintegration. *Phys. Rev.*, 48:512–516, 1935, [doi:10.1103/PhysRev.48.512](#).
- [10] M. G. Inghram and J. H. Reynolds. Double beta-decay of  $^{130}\text{Te}$ . *Phys. Rev.*, 78(6):822–823, June 1950, [doi:10.1103/PhysRev.78.822.2](#).
- [11] J. A. Kadyk. Wire chamber aging. *Nucl. Instrum. Meth.*, A300:436–479, 1991, [doi:10.1016/0168-9002\(91\)90381-Y](#).
- [12] H. V. Klapdor-Kleingrothaus, I. V. Krivosheina, A. Dietz, and O. Chkvorets. Search for neutrinoless double beta decay with enriched Ge-76 in Gran Sasso 1990–2003. *Phys. Lett.*, B586:198–212, 2004, [hep-ph/0404088](#).
- [13] G. F. Knoll. *Radiation detection and measurement*. John Wiley & Sons, Inc., third edition, 2000.

- [14] S. A. Korff and R. D. Present. On the role of polyatomic gases in fast counters. *Phys. Rev.*, 65(9-10):274–282, May 1944, [doi:10.1103/PhysRev.65.274](https://doi.org/10.1103/PhysRev.65.274).
- [15] J. Mylroie-Smith. Studies of a prototype tracker for the double beta decay experiment SuperNEMO. Master’s thesis, School of Physics and Astronomy, Manchester, September 2007.
- [16] G. M. Forker N. A. Lange. *Lange’s Handbook of Chemistry*. McGraw-Hill Book Company, 10th edition, 1967.
- [17] W. Rodejohann. Leptogenesis, neutrinoless double beta decay and terrestrial CP violation. *Acta Phys. Polon.*, B32:3845–3854, 2001, [hep-ph/0110258](https://arxiv.org/abs/hep-ph/0110258).
- [18] S. Snow. The University of Manchester, private communication, 2007.
- [19] D. H. Wilkinson. The Geiger discharge. *Phys. Rev.*, 74(10):1417–1429, 1948, [doi:10.1103/PhysRev.74.1417](https://doi.org/10.1103/PhysRev.74.1417).
- [20] D. H. Wilkinson. The geiger discharge revisited. 1. the charge generated. *Nucl. Instrum. Meth.*, A321:195–210, 1992, [doi:10.1016/0168-9002\(92\)90388-K](https://doi.org/10.1016/0168-9002(92)90388-K).
- [21] W. M. Yao et al. Review of particle physics. *J. Phys.*, G33:1–1232, 2006, [doi:10.1088/0954-3899/33/1/001](https://doi.org/10.1088/0954-3899/33/1/001).